

# Genesis, structural, and transport properties of $\text{La}_2\text{Mo}_{2-x}\text{W}_x\text{O}_9$ prepared via mechanochemical activation

S. Pavlova<sup>1</sup> · Y. Bespalko<sup>1</sup> · T. Krieger<sup>1</sup> · V. Sadykov<sup>1,2</sup> · N. Uvarov<sup>3</sup>

Received: 9 June 2016 / Revised: 14 September 2016 / Accepted: 13 October 2016 / Published online: 3 November 2016  
© Springer-Verlag Berlin Heidelberg 2016

**Abstract** Fast oxide-ion conductors  $\text{La}_2\text{Mo}_{2-x}\text{W}_x\text{O}_9$  ( $x = 0–1$ ) have been prepared using mechanochemical activation (MA) of starting oxides in a high-power planetary ball mill. Studies of  $\text{La}_2\text{Mo}_{2-x}\text{W}_x\text{O}_9$  genesis and structural properties using thermal analysis, XRD, SEM, IR, and Raman spectroscopy have revealed that MA results in the formation of an amorphous precursor, while the cubic  $\beta$ -phase is formed after calcination at 700–900 °C. Due to a high dispersion of powders, high-density pellets of W-LAMOX ceramics have been obtained already after sintering at 950 °C. Their electrical conductivity measured by the impedance spectroscopy depends on the W concentration being sufficiently high (up to  $5.6 \cdot 10^{-3}$  S/cm at 630 °C) at temperatures below 650 °C.

**Keywords** Doping · Ionic conductivities · Materials preparations · XRD · FTIR

## Introduction

The family of fast oxide-ion conductors based on  $\text{La}_2\text{Mo}_2\text{O}_9$  (so-called LAMOX) has attracted a considerable interest due to their possible application in solid oxide fuel cells operating at intermediate temperatures [1–5]. Their high anionic conductivity is provided by a high concentration of intrinsic

oxygen vacancies in the crystal lattice required for the fast oxygen ion diffusion. However, for parent  $\text{La}_2\text{Mo}_2\text{O}_9$ , a phase transition from a cubic high-temperature  $\beta$  form to a monoclinic low-temperature  $\alpha$  phase observed at about 580 °C leads to an abrupt decrease of conductivity by almost two orders of magnitude [1–3, 6]. Another problem hampering LAMOX application is their poor phase stability at low oxygen concentrations or in reducing conditions [3–5]. Doping of  $\text{La}_2\text{Mo}_2\text{O}_9$  with different cations in La sites (alkaline [7], alkaline-earth [8, 9], rare-earth [10, 11], Bi [12]) was shown to stabilize a highly conductive  $\beta$  phase to room temperature while substitution of Mo with W not only stabilizes  $\beta$  phase but considerably improves LAMOX stability under reducing conditions as well [13–23].

W-doped LAMOX oxides are usually prepared by the solid-state method, which requires prolonged heating at high temperatures with the intermediate homogenization of the powder precursors to obtain a target phase and dense ceramics [13–17]. Besides, such procedures cause losses of Mo and W due to a high volatility of their oxides that result in formation of multiphase products. There are only several works in the literature devoted to W-LAMOX synthesis by microwave method [18], Pechini method [19], freeze drying [20, 21], and spray pyrolysis [22]. These methods usually involve several steps which take many hours to achieve the complete mixed oxide phase formation or require special complex equipment. Besides, productivity of “wet” methods including Pechini route is limited by a low solubility of raw tungsten salts [24].

The alternative route to avoid these problems is using high-energy milling of starting oxides [25–27]. During milling, a high-energy input into the reaction zone generates defects in solids up to their amorphization and transfer of compounds into so-called «atom-ionic state» that greatly accelerate the chemical interaction between solids. The raw compounds

✉ S. Pavlova  
pavlova@catalysis.ru

<sup>1</sup> Borekov Institute of Catalysis SB RAS, Pr. Lavrentieva, 5, Novosibirsk, Russian Federation 630090

<sup>2</sup> Novosibirsk State University, Novosibirsk, Russian Federation

<sup>3</sup> Institute of Solid State Chemistry SB RAS, Novosibirsk, Russian Federation

can form target products directly during milling or they can be transformed into precursors. In the first case, the term “mechanochemical synthesis” (MS) is usually used while the term “mechanochemical activation” (MA) can be used if only precursors are formed. MS(MA) is an environmentally friendly method due to absence of any wastes. Such approach was proved to be very efficient in synthesis of complex oxides of different types: perovskites, fluorites, pyrochlores, apatites, etc. [25–27]. Among LAMOX, only the undoped  $\text{La}_2\text{Mo}_2\text{O}_9$  was obtained by MS after milling of  $\text{La}_2\text{O}_3$  and  $\text{MoO}_3$  mixture during 12 h [28]. For W-doped LAMOX, ball milling has been used only for production of powders to prepare dense ceramics from  $\text{La}_{2-x}\text{R}_x\text{Mo}_{2-y}\text{W}_y\text{O}_9$  (R: Nd, Gd, Y) samples obtained by solid-state reaction [29].

In this work,  $\text{La}_2\text{Mo}_{2-x}\text{W}_x\text{O}_9$  ( $x = 0-1$ ) oxides have been prepared using high-energy milling (mechanochemical activation) of starting oxides in a high-energy planetary ball mill AGO-2. The results of the study of LAMOX genesis during milling and subsequent annealing of its products as well as the effect of the partial substitutions of  $\text{Mo}^{6+}$  by  $\text{W}^{6+}$  cations in  $\text{La}_2\text{Mo}_2\text{O}_9$  on structural and electrical properties are presented.

## Experimental

### Synthesis

To synthesize  $\text{La}_2\text{Mo}_{2-x}\text{W}_x\text{O}_9$  ( $y = 0-1$ ), the mechanical milling of La, Mo, and W oxides was used. Lanthanum oxide contained admixtures of lanthanum hydroxide and oxycarbonate as revealed by XRD analysis. Mo and W oxides were obtained via calcination of  $(\text{NH}_4)_6\text{Mo}_7\text{O}_{24}\cdot 6\text{H}_2\text{O}$  and  $(\text{NH}_4)_6\text{W}_7\text{O}_{24}\cdot 6\text{H}_2\text{O}$  mixture at 270 °C for 4 h to prevent evaporation of molybdenum oxide [24]. To provide a target stoichiometry of samples, corresponding amounts of starting compounds were taken on the basis of their thermal analysis. For  $\text{La}_2\text{O}_3$ , the analysis was conducted up to 1200 °C that ensured decomposition of oxycarbonate and removal of hydroxyls.

Stoichiometric mixtures of oxides were milled in the high-energy planetary ball mill AGO-2 with two steel drums (150 ml volume) at 1200 rpm rotation rate. The steel ball diameter was 8 mm, and ball-to-sample mass ratio was 20. The time of milling was 1–30 min in the study of  $\text{La}_2\text{MoWO}_9$  genesis during mechanical activation (MA), and it was 15 min for synthesis of two other samples. In each experiment of MA genesis study, the same fresh portion of a given starting mixture was milled for respective time period (1 or 5, 10, 15, 20, 30 min). Before each synthesis, a preliminary treatment of steel drums and balls with the corresponding mixture was performed to minimize contamination of samples with Fe. As a result,

the surface of drums and balls was covered by a layer of the initial mixture. Such procedure was earlier shown to decrease the amount of Fe in MA products below  $0.05 \pm 0.01$  wt% [30]. For the study of LAMOX formation under annealing, the starting mixture of oxides corresponding to  $\text{La}_2\text{MoWO}_9$  was milled during 15 min and the MA products were calcined at 550–950 °C. The products obtained after each experiment (MA or annealing) were studied by XRD, IR, and Raman spectroscopy.

The chemical composition of all samples and their abbreviations are presented in Table I.

### Characterization

The genesis of prepared LAMOX and their structural properties were studied by thermal analysis, XRD, SEM, IR, and Raman spectroscopy. X-ray diffraction patterns were recorded at room temperature with a D8 Advance diffractometer (Bruker, Germany) using  $\text{CuK}\alpha$  radiation in  $2\theta$  scanning range 15–80° with step 0.05°. Qualitative phase analysis has been carried out by using PDF-2–ICDD files and ICSD/retrieve database. Thermal analysis (DTA/TG) of LAMOX was carried out with a Simultaneous DTA-TG Apparatus DTG-60H SHIMADZU in the flow of air (30 ml/min) at a heating rate of 10 °C/min. Particle size distribution of powdered samples calcined at 700 °C was determined using laser diffraction particle size distribution analyzer SALD 2101 (Shimadzu Corp., Japan) (measuring range: 0.03–1000  $\mu\text{m}$ ) equipped with a batch cell. Data processing was carried out using the standard data processing program “Wing-1.” For analysis, the suspension of the sample in Na-H.M.P. solution was stirred with a magnetic stirrer for 5 min and then subjected to ultrasonic treatment at 35 kHz frequency for 3 min. Microstructural characterization and EDX analysis of powdered samples and sintered pellets were carried out with Tesla BS-350 scanning electron microscope.

FTIR spectra were recorded in the range of 200–4000  $\text{cm}^{-1}$  using a BOMEM MB-102 FT-IR spectrometer. The samples were pre-treated by a standard method that involved pelletizing the powder with CsI (2 mg of a sample and 500 mg of CsI). FT-Raman spectra (3600–100  $\text{cm}^{-1}$ , 300 scans, resolution 4  $\text{cm}^{-1}$ , 180° geometry) were recorded using a RFS 100/S Bruker spectrometer. Excitation of the 1064-nm line was provided by a Nd:YAG laser (100 mW power output).

For electrical characterization, LAMOX powders calcined at 700 °C were pressed into pellets (diameter 15 mm, thickness 1 mm) under  $\sim 150$  kgf/cm<sup>2</sup> and sintered at 950 °C for 6 h. The impedance spectroscopy was used to study a total conductivity of the sintered pellets. Both of their sides were coated with silver paste to form

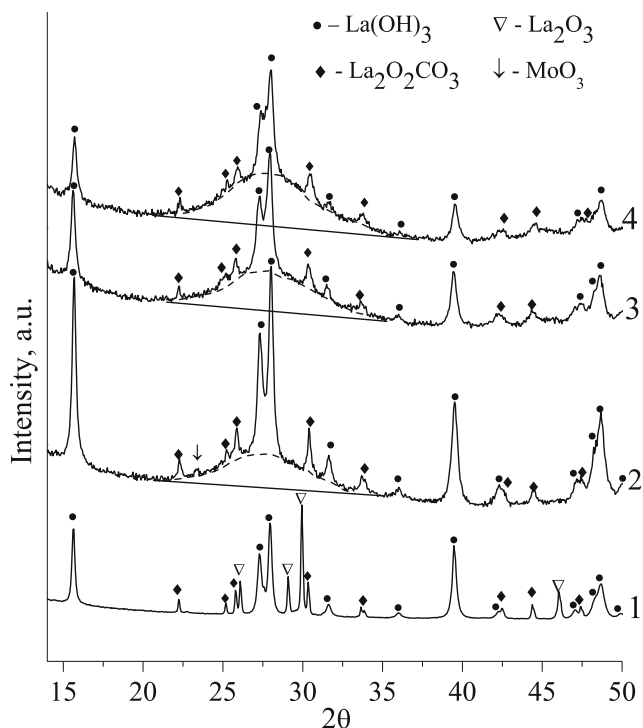


**Fig. 1** XRD patterns of milling products after different times of mechanochemical activation for LaMoWO<sub>9</sub>. 1 – starting La<sub>2</sub>O<sub>3</sub>, 2–5 min, 3–15 min, 4–30 min

electrodes. The measurements were carried out at 250 to 650 °C in air using a MNIPI E7–25 Meter at potential value of 10 mV in the frequency range 25 Hz–1 MHz. The specific conductivities ( $\sigma$ ) were calculated by simulating the experimental impedance spectra using the equivalent electric circuit method [20].

## Results and discussion

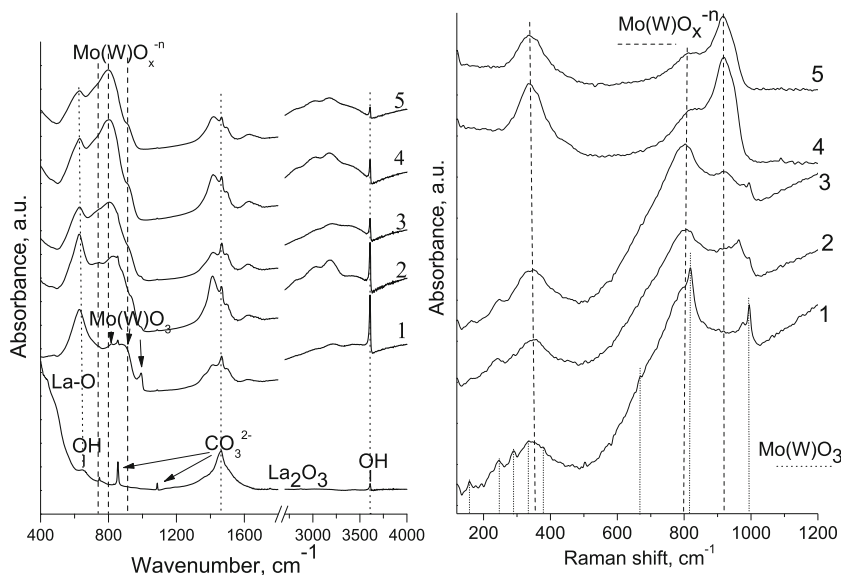
### Genesis of phase composition

The genesis of La<sub>2</sub>Mo<sub>2-x</sub>W<sub>x</sub>O<sub>9</sub> at different synthesis stages (during mechanical activation and subsequent calcinations) has been studied in detail for the sample with  $x = 1$ .

XRD patterns of starting lanthanum oxide and mechanical activation products are presented in Fig. 1. According to XRD data, starting lanthanum oxide contains admixtures of hexagonal La(OH)<sub>3</sub> and La<sub>2</sub>O<sub>2</sub>CO<sub>3</sub>. XRD patterns of MA products show a gradual interaction of starting oxides during activation. Thus, after 5 min, a halo in the 2 $\theta$  range of 20–35° corresponding to amorphous phase appears. Simultaneously, hydration of lanthanum oxide with formation of hydroxide occurs. There is only one weak reflection of molybdenum oxide at 2 $\theta$  ~23.37° in the pattern while reflections of tungsten oxide are absent. At increasing milling time, intensity of lanthanum hydroxide diffraction peaks declines and peak corresponding to molybdenum oxide disappears, while halo of the amorphous phase rises by intensity. Note that after 30 min of activation, reflections of lanthanum hydroxide and oxycarbonate are still observed.

Infrared and Raman spectra give additional data on formation of amorphous phase and its nature (Fig. 2). The IR spectrum of the starting lanthanum oxide shows a broad intense band at 400–600 cm<sup>-1</sup> corresponding to vibrations of La-O in La<sub>2</sub>O<sub>3</sub> [31], while the bands at 645 and 3610 cm<sup>-1</sup> are related to the bending and stretching OH-group vibrations of lanthanum hydroxide [32]. The narrow bands at 746, 853, 1089 and a broad band in the range of 1280–1650 cm<sup>-1</sup> with the maximum at 1464 cm<sup>-1</sup> correspond to stretching and bending

**Fig. 2** IR (left) and Raman (right) spectra of milling products after different times of mechanochemical activation for LaMoWO<sub>9</sub>. 1–1 min, 2–5 min, 3–10 min, 4–15 min, 5–30 min



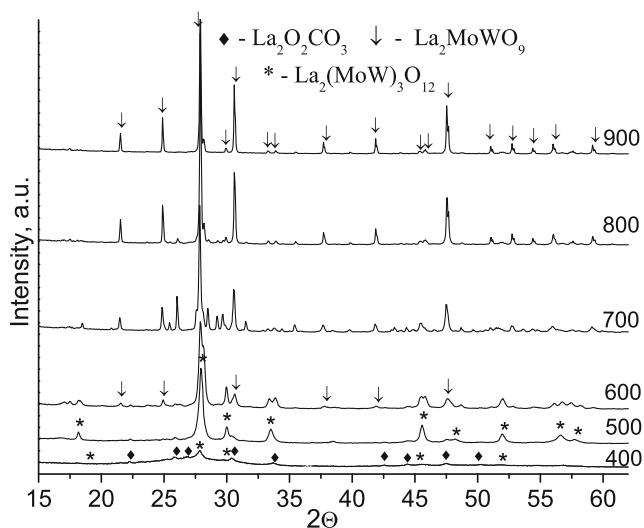


**Fig. 3** XRD patterns of LaMoWO<sub>9</sub> after calcination of milling products at 400–900 °C

vibrations of carbonate ion in La<sub>2</sub>O<sub>2</sub>CO<sub>3</sub> [31, 33]. The presence of lanthanum hydroxide and oxycarbonate in the starting material is explained by the fact that the sesquioxides of rare earth elements and their hydroxides are strongly subjected to hydration and carbonization being exposed to atmospheric CO<sub>2</sub> and H<sub>2</sub>O at room temperature and standard pressure [34, 35].

After 1 min milling, the band corresponding to La<sub>2</sub>O<sub>3</sub> disappears in the IR spectrum of products while the intensity of bands at 645 and 3610 cm<sup>-1</sup> related to bending and stretching vibrations of OH-groups in La(OH)<sub>3</sub> increases as a result of lanthanum oxide hydration (Fig. 2, left). The bands at 995, 880, and 820 cm<sup>-1</sup> correspond to stretching vibrations of different Mo(W)-O bonds in starting oxides [36–39]. The bands

at 1495, 1465, 1365, 1085 (stretching vibrations), and 855 cm<sup>-1</sup> (bending vibrations ν<sub>4</sub>) correspond to carbonate ion in La<sub>2</sub>O<sub>2</sub>CO<sub>3</sub>. The bands at 3400 and 1625 cm<sup>-1</sup> are assigned to stretching and bending vibrations of OH group in water. Besides, the bands at 3190, 3030, 2850 (stretching vibrations ν<sub>3</sub>), and 1415 cm<sup>-1</sup> (bending vibrations ν<sub>4</sub>) of NH<sub>4</sub><sup>+</sup> remained from precursors salts are also observed.

At further milling for 5–30 min, the intensity of bands corresponding to La(OH)<sub>3</sub> decreases, showing its partial consumption, while the bands assigned to Mo(W)-O vibrations in initial oxides also reduce in intensity and disappear after milling for 13 min. Simultaneously, bands at 910, 800, 740, and 640 cm<sup>-1</sup> corresponding to molybdates and tungstates [40, 41] appear evidencing formation of a new compound. The bands assigned to carbonate ion in crystalline La<sub>2</sub>O<sub>2</sub>CO<sub>3</sub> are reduced by intensity during milling, but their presence even after 30 min of treatment shows, in agreement with XRD data, only partial decomposition of lanthanum oxycarbonate with simultaneous formation of surface carbonates characterized by the broad bands at ~1410 and 1495 cm<sup>-1</sup>.

Raman spectra widely used for studies of Mo(W)-based compounds [36–44] allow to explore, in more details, transformation of products during mechanical activation. In the Raman spectra of the sample milled for 1 min, two groups of bands are observed. The bands between 150 and 400 cm<sup>-1</sup> (at 290, 245, and 155 cm<sup>-1</sup>) are associated with Mo(W)-O bending vibrations, while the high frequency bands at 995, 820, and 665 cm<sup>-1</sup> correspond to stretching vibrations of Mo(W)-O in Mo(W)O<sub>3</sub> [36–39, 41–44]. The bands of a low intensity at 975, 795, and 350 cm<sup>-1</sup> corresponding to molybdates and tungstates [40, 41] are also observed in the spectrum, probably, due to incomplete decomposition of these starting compounds after calcination at 270 °C. The intensity

**Fig. 4** IR (left) and Raman (right) spectra of LaMoWO<sub>9</sub> after calcination of MA products: 1–400°, 2–500°, 3–600°, 4–700°, 5–800 °C, 6–900 °C

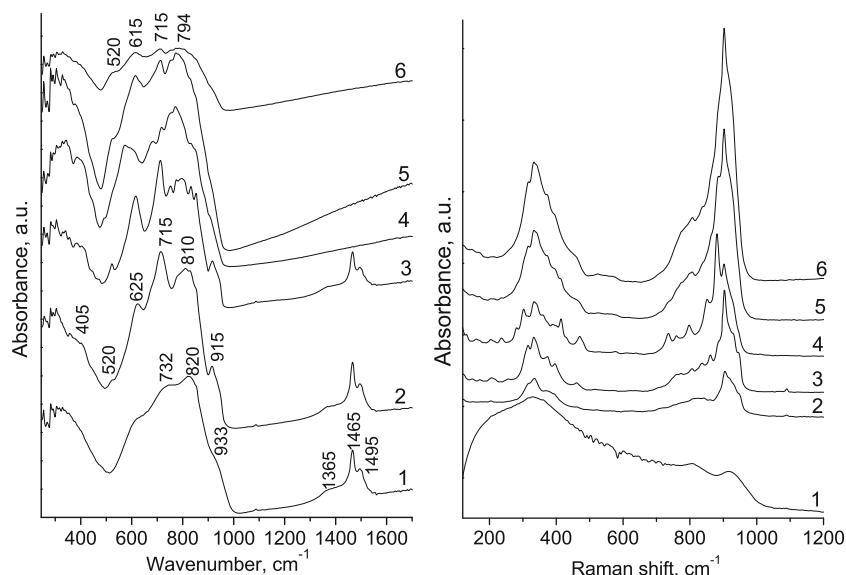
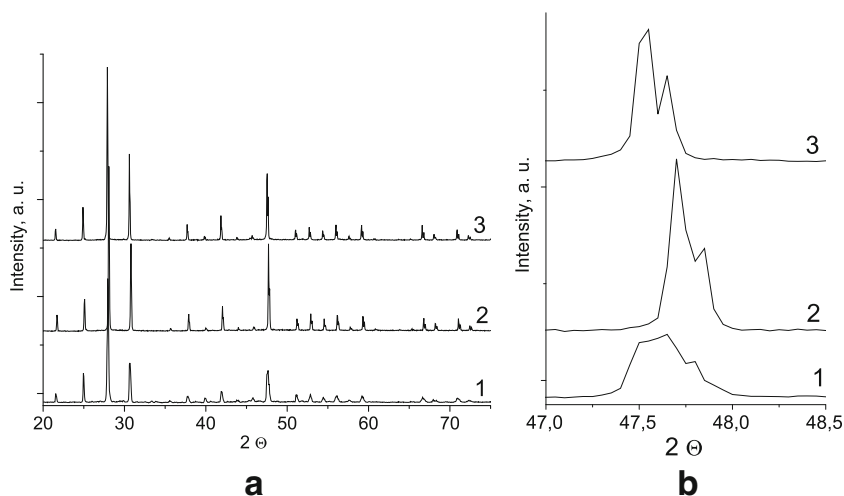


**Fig. 5** XRD patterns of pellets after calcination of MA products at 950 °C (**a**) and enlarged region at  $2\theta = 47\text{--}48^\circ$  (**b**). 1:  $\text{La}_2\text{Mo}_2\text{O}_9$ , 2:  $\text{La}_2\text{Mo}_{1.5}\text{W}_{0.5}\text{O}_9$ , 3:  $\text{La}_2\text{MoWO}_9$ . All reflections correspond to the LAMOX phase



of starting oxides bands decreases after milling for 5–10 min, and they disappear after milling for 15 min. Simultaneously, the intensity of molybdates (tungstates) bands at  $330\text{--}360\text{ cm}^{-1}$  (bending vibrations of Mo(W)-O bond ( $\nu_2$  and  $\nu_4$ )) and  $795\text{--}810\text{ cm}^{-1}$  (stretching vibrations ( $\nu_3$ )) increases, and the band at  $915\text{--}920\text{ cm}^{-1}$  (asymmetric stretching vibrations ( $\nu_1$ )) [41–44] appears after 10 min milling. The changes in the intensity of  $\nu_1$  and  $\nu_3$  bands could be due to interaction of components in the course of milling and formation of mixed lanthanum molybdate–tungstate oxide. The exact assignment of bands to either molybdate or tungstate is difficult due to their large width and close position of individual bands [40, 44, 45].

Formation of  $\text{La}_2\text{MoWO}_9$  during annealing of the amorphous precursor obtained after 15 min milling has been studied by XRD, IR, and Raman spectroscopy. According to XRD data (Fig. 3), calcination of milling products at 400 °C leads to disappearance of remaining unreacted  $\text{La}(\text{OH})_3$ , retaining of the amorphous phase and lanthanum oxycarbonate, and appearance of a weak reflection at  $2\theta \sim 27.86^\circ$ . After annealing at 500 °C, the halo of the amorphous phase disappears while the intensity of the reflection at  $2\theta \sim 27.86^\circ$  increases and a number of additional reflections emerges. In general, these reflections correspond to the pattern of  $\text{La}_2\text{Mo}_3\text{O}_{12}$  (JCPDS 26–0821), though some shifts of several peaks are observed due to formation of  $\text{La}_2(\text{MoW})_3\text{O}_{12}$  mixed oxide. The formation of  $\text{La}_2\text{Mo}_3\text{O}_{12}$  as an intermediate compound during synthesis of  $\text{La}_2\text{Mo}_2\text{O}_9$  has been observed in previous work [46]. At 600 °C, weak reflections of  $\text{La}_2\text{MoWO}_9$  additionally appear. After calcination at 700 °C, the main phase is the target LAMOX with the admixture of  $\text{La}_2(\text{MoW})_3\text{O}_{12}$  provided by interaction between  $\text{La}_2(\text{MoW})_3\text{O}_{12}$  and remaining lanthanum oxycarbonate. Increasing annealing temperature up to 900 °C results in formation of single-phase  $\text{La}_2\text{MoWO}_9$  sample.

Infra-red spectra (Fig. 4, left) agree with X-ray diffraction data and add information on the genesis of target LAMOX during annealing of the amorphous precursor. Thus, after calcination at 400 °C, the bands at 645 and  $3610\text{ cm}^{-1}$  related to  $\delta(\text{La-OH})$  and  $\nu(\text{OH})$  vibrations in  $\text{La}(\text{OH})_3$  [31, 32] disappear while the bands at 1495, 1465, and  $1365\text{ cm}^{-1}$  show the presence of  $\text{La}_2\text{O}_2\text{CO}_3$  [33–35] in agreement with XRD data. The bands in the range of  $600\text{--}900\text{ cm}^{-1}$  ( $732, 820, 933\text{ cm}^{-1}$ ) corresponding to amorphous mixed molybdate–tungstate [40, 44, 45] are slightly shifted with changing their relative intensities, thus evidencing distortion of Mo(W)- $\text{O}_x$  polyhedra. These bands disappear after calcination at 500 °C, showing complete transformation of the amorphous phase into a new phase characterized by a number of bands in both low and high frequency regions, the most intensive ones being situated at 915, 810, 715, 625, 520, and  $405\text{ cm}^{-1}$ . On

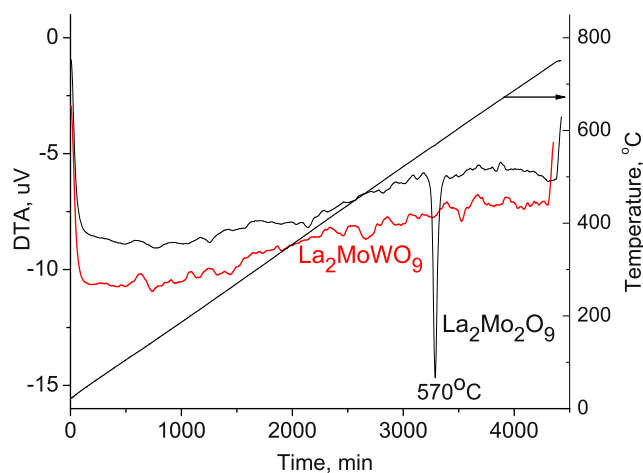


**Fig. 6** DTA thermograms of  $\text{La}_2\text{Mo}_2\text{O}_9$  and  $\text{La}_2\text{MoWO}_9$ , calcined at 950 °C

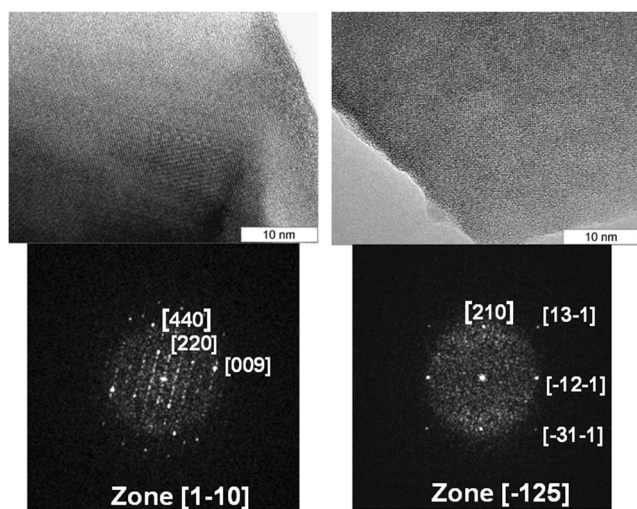


**Fig. 7** TEM image and electron diffraction patterns of  $\text{La}_2\text{Mo}_2\text{O}_9$  (left) and LMW (right)

the whole, the spectra are similar to that of  $\text{La}_2\text{Mo}_3\text{O}_{12}$  phase [47]; however, some differences in the bands intensity and positions are observed due to formation of a mixed  $\text{La}_2(\text{MoW})_3\text{O}_{12}$  oxide. Annealing at 600 °C leads to a slight shifting of bands, their narrowing, and increase in intensity along with a higher splitting, thus evidencing perfection of the structure. After calcination at 700 °C, the bands of lanthanum oxycarbonate completely disappear while the band alterations and appearance of new bands in the region corresponding to vibrations of Mo(W)-O polyhedra show partial decomposition of  $\text{La}_2(\text{MoW})_3\text{O}_{12}$  along with formation of target  $\text{La}_2\text{MoWO}_9$  phase. Annealing at 900 °C results in disappearance of bands at 719, 750, 773, and 838  $\text{cm}^{-1}$  assigned to  $\text{La}_2(\text{MoW})_3\text{O}_{12}$  [47], and the spectrum showing a.b. at 520, 615, 715, 795  $\text{cm}^{-1}$  becomes close to those typical for  $\text{La}_2\text{Mo}_2\text{O}_9$  [48].

Raman spectra show evolution of amorphous mixed molybdate–tungstate during annealing (Fig. 4, right). The spectrum of sample calcined at 400 °C is a broad band due to a distortion of Mo(W)- $\text{O}_x$  polyhedra as agrees

**Fig. 8** SEM image (left) and particles size distribution (right) for the powder of  $\text{La}_2\text{MoWO}_9$  calcined at 700 °C

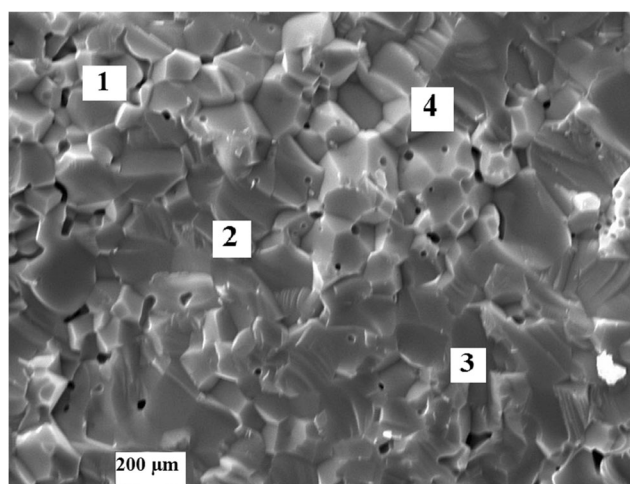
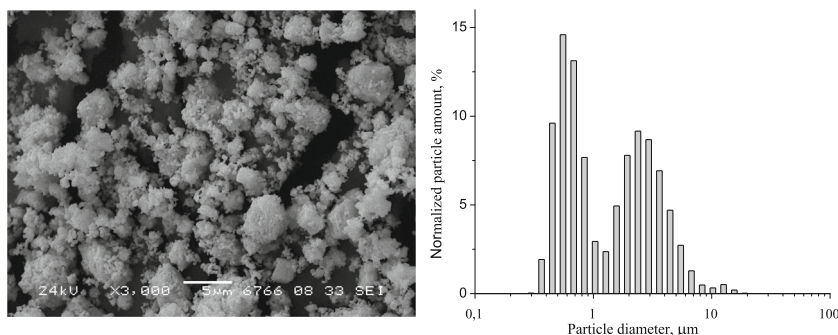
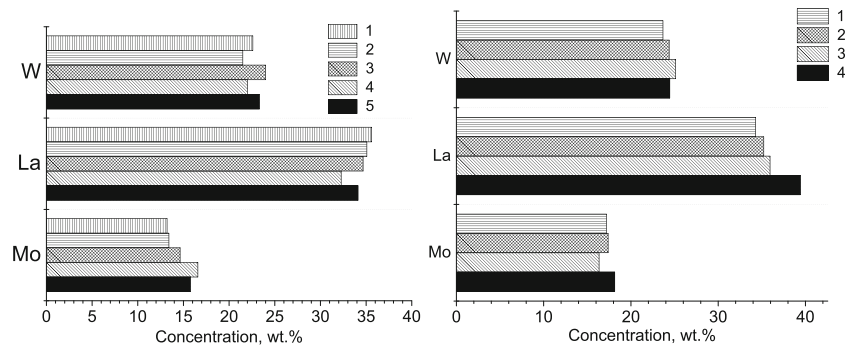


**Fig. 9** SEM image of unpolished surface of the  $\text{La}_2\text{Mo}_{0.5}\text{W}_{0.5}\text{O}_9$  pellet annealed at 950 °C. EDX analysis was carried out at the points 1–4 (see Fig. 10, right)

with IR data. After calcination at 500 °C, a number of bands with a low intensity appear in the low and high frequency regions corresponding to bending and stretching vibrations of Mo(W)-O bonds close to the ones in  $\text{La}_2\text{Mo}_3\text{O}_{12}$ . Annealing at 600–700 °C leads to pronounced splitting of the bands that is a characteristic feature of monoclinic  $\text{La}_2\text{Mo}_3\text{O}_{12}$  [49]. Simultaneously, some changes in position and intensity of the bands evidence the starting formation of the target  $\text{La}_2\text{MoWO}_9$ . After calcinations at 800–900 °C, bands splitting disappears showing complete consumption of  $\text{La}_2(\text{MoW})_3\text{O}_{12}$ , and the spectra become close to that for  $\text{La}_2\text{Mo}_2\text{O}_9$  [18]. A reliable interpretation of bands in the spectra of  $\text{La}_2(\text{MoW})_3\text{O}_{12}$  and  $\text{La}_2\text{Mo}_2\text{O}_9$  is difficult due to strong couplings of different polyhedral vibrations in the lattice as considered in [17, 18].

Thus, our results have shown that though the target tungsten doped molybdates are not formed directly during mechanical activation, it facilitates formation of the single phase LAMOX. The XRD patterns of  $\text{La}_2\text{Mo}_2\text{O}_9$  and

**Fig. 10** EDX analysis: concentration of La, Mo, and W in the different points of the samples: the powder of  $\text{La}_2\text{MoWO}_9$  calcined at  $700\text{ }^\circ\text{C}$  (left) and the tablet of  $\text{La}_2\text{Mo}_{1.5}\text{W}_{0.5}\text{O}_9$  annealed at  $950\text{ }^\circ\text{C}$  (right)



$\text{La}_2\text{Mo}_{2-x}\text{W}_x\text{O}_9$  pellets obtained after calcination of MA products at  $950\text{ }^\circ\text{C}$  (Fig. 5) show only reflections of LAMOX.

### Structural properties

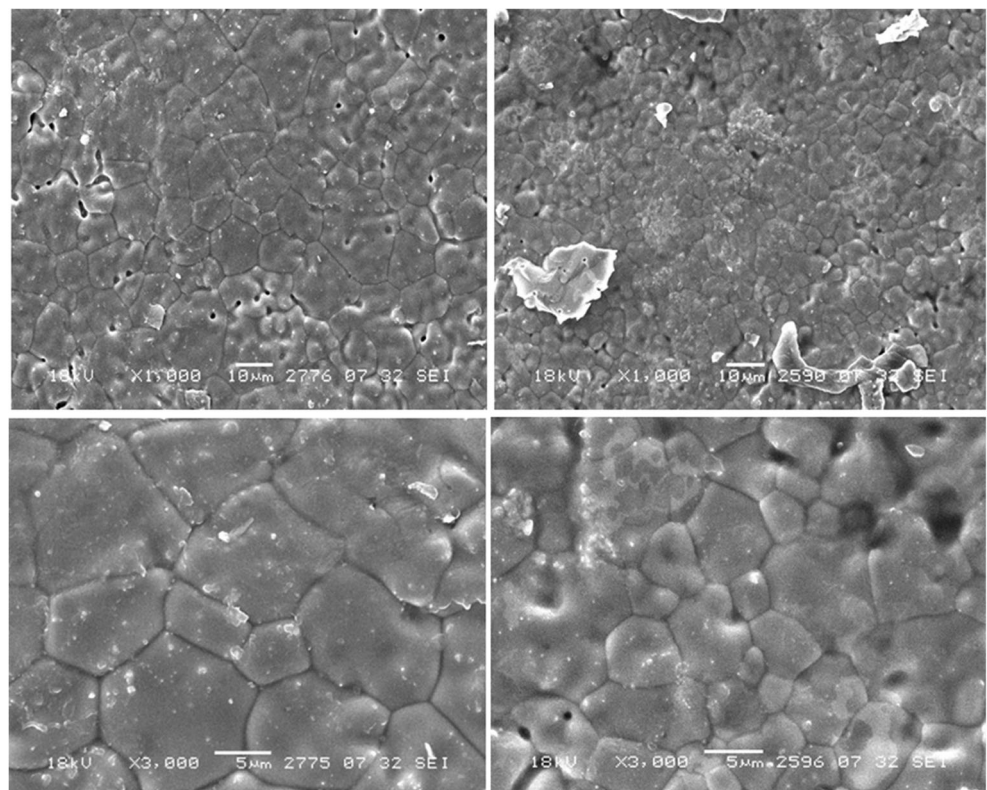
It is known that  $\text{La}_2\text{Mo}_2\text{O}_9$  crystallizes in two different forms: a low-temperature  $\alpha$  phase and a high-temperature  $\beta$ -form. The high-temperature  $\beta$  form has a cubic structure (space group P213), and the  $\alpha$ -phase is considered as a slight monoclinic distortion of the  $\beta$ -form [1–6]. The differences in the XRD patterns of these two phases are minimal, and the monoclinic distortion results in the presence of a few extra peaks with a low intensity and in the splitting of some pseudo-cubic (111), (201), (211) and (321) reflections. The most sensitive to

a monoclinic distortion of the  $\beta$ -phase is the (321) reflection in the  $2\theta$  range of  $47\text{--}48^\circ$ . Therefore, the analysis of its shape could be used for the preliminary determination of the doped LAMOX structure and estimation of the cubic phase stabilization at room temperature by various dopants.

The enlarged (321) reflections for pellets calcined at  $950\text{ }^\circ\text{C}$  are shown in Fig. 5. In the case of undoped  $\text{La}_2\text{Mo}_2\text{O}_9$ , the (321) reflection is a broad line with some splitting that is a characteristic feature of monoclinic  $\alpha$ -phase. The (321) reflection of W-doped LAMOX is a sufficiently narrow line which is typical for high-temperature cubic  $\beta$ -phase evidencing its retention at room temperature.

Additionally, the thermal analysis of samples calcined at  $900\text{ }^\circ\text{C}$  has been conducted. The DTA thermogram of undoped  $\text{La}_2\text{Mo}_2\text{O}_9$  (Fig. 6) shows an endothermic peak at

**Fig. 11** SEM image of  $\text{La}_2\text{Mo}_2\text{O}_9$  (left) and LMW (right) pellets sintered at  $950\text{ }^\circ\text{C}$  at different magnification



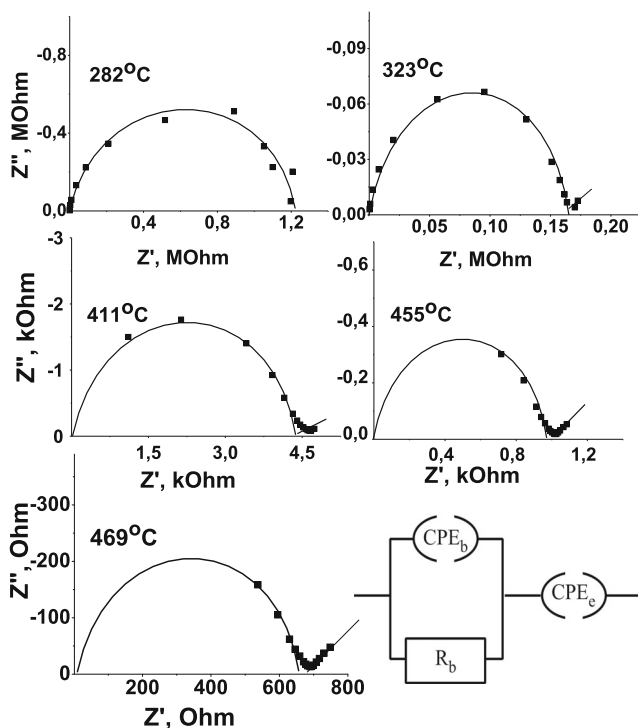


**Fig. 12** Impedance plots for  $\text{LaMoWO}_9$  obtained at different temperatures and the equivalent circuit used for the data interpretation, where the bulk impedance:  $R_b$  (the bulk resistance) and  $(CPE)_b$  (the constant phase element), the electrode impedance  $(CPE)_e$  (the constant phase element)

about  $570^\circ\text{C}$  corresponding to the structural  $\alpha \rightarrow \beta$  transition [1–6], while any endothermic peaks are absent for W-doped sample. Thus, the data of the thermal analysis also confirm

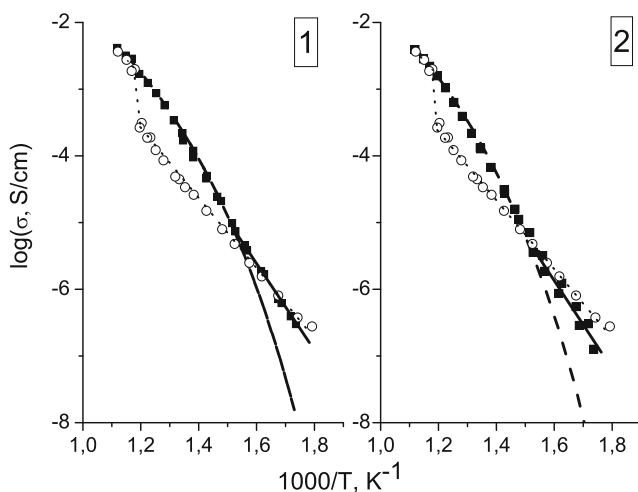


**Fig. 13** Arrhenius plots of conductivity for  $\text{LaMoWO}_3$  (1) and  $\text{La}_2\text{Mo}_{1.5}\text{W}_{0.5}\text{O}_9$  (2) fitted with a conventional Arrhenius model at low temperature (solid lines) and with a VTF model at high temperature (dash lines). Dot lines with hollow circles correspond to conductivity of  $\text{La}_2\text{Mo}_2\text{O}_9$  as a reference

stabilization of cubic structure in W-doped LAMOX. Stabilization of the cubic phase is also confirmed by TEM data (Fig. 7). In the electron diffraction pattern of undoped  $\text{La}_2\text{Mo}_2\text{O}_9$ , positions of reflections and interplanar spaces correspond to monoclinic  $\alpha\text{-La}_2\text{Mo}_2\text{O}_9$  (ICSD 172479) [13]. Electron diffraction patterns of LMW show reflections and interplanar spaces close to those for cubic  $\beta\text{-La}_2\text{Mo}_2\text{O}_9$  phase (ICSD 98871) [6, 12].

The unit cell parameter of  $\text{La}_2\text{MoWO}_9$  estimated from XRD data is a little larger as compared with that for undoped  $\text{La}_2\text{Mo}_2\text{O}_9$  (0.7156(9) and 0.7149(3) nm, respectively) due to a slightly larger ionic radius of  $\text{W}^{6+}$  (0.6 Å) versus that of  $\text{Mo}^{6+}$  cation (0.59 Å) in agreement with the literature data [13, 14, 16].

The structure of  $\beta\text{-LAMOX}$  is considered to be a rigid framework built up by  $[\text{O}1(\text{La})_3\text{Mo}]$  tetrahedra surrounded by partially occupied O2 and O3 oxygen sites [2, 3, 6]. According to structural studies of  $\text{La}_2\text{Mo}_2\text{O}_9$  by neutron powder diffraction, there is a substantial disorder in the oxygen sublattice of  $\beta$ -phase, which is considered to determine a high-oxygen mobility [2, 3, 6]. Doping  $\text{La}_2\text{Mo}_2\text{O}_9$  with tungsten, along with a slight increase of the unit cell, results in alteration of O2 and O3 site occupation leading to a higher disordering [13, 16].

## SEM analysis

The SEM image and particle size distribution for the powder of  $\text{LaMoWO}_9$  calcined at  $700^\circ\text{C}$  are presented in Fig. 8. The SEM image shows presence of separate particles of a small size along with large aggregates. According to the analysis of the particles size distribution, it is in the range of 0.35–15 μm. The histogram passes through the two maxima at 0.54 and 2.4 μm. EDX analysis of the powdered  $\text{LaMoWO}_9$  and the pellet of  $\text{La}_2\text{Mo}_{1.5}\text{W}_{0.5}\text{O}_9$  sintered at  $950^\circ\text{C}$  shows sufficiently uniform distribution of La, Mo, and W in both samples (Fig. 9–10).

The SEM images of  $\text{La}_2\text{Mo}_2\text{O}_9$  and  $\text{LaMoWO}_9$  pellets sintered at  $950^\circ\text{C}$  are presented in Fig. 11 and show a low porosity with a high (>95 %) apparent density and well-connected grains. Besides, the size of grains for  $\text{LaMoWO}_9$  is noticeably smaller as compared with those for undoped  $\text{La}_2\text{Mo}_2\text{O}_9$ . Thus, in agreement with previous works [14, 49], W doping hampers the grain growth of LAMOX.

## Conductivity

The conductivity measurements were carried out for pellets sintered at  $950^\circ\text{C}$ . The impedance spectra of sintered samples are typical for ionic conductors (Fig. 12). All  $Z'' = f(Z')$  dependences may be satisfactorily described by an equivalent scheme which includes the bulk and electrode impedances connected in series (Fig. 12). The bulk impedance includes



**Table 1** Chemical and phase composition, conductivity ( $\sigma$ ), and activation energy ( $E_{\text{act}}$ ) of LAMOX samples prepared via mechanochemical activation followed by annealing at 700–900 °C

Sample	Stoichiometry	Phase composition <sup>a</sup>		$\sigma^b$ , 10 <sup>-3</sup> Sm/ cm	$E_{\text{act}}^c$ , eV	$E_{\text{act}}^d$ V
		700 °C	900 °C			
LM	La <sub>2</sub> Mo <sub>2</sub> O <sub>9</sub>	$\alpha$ -phase		4.2	1.1	–
LMW <sub>0.5</sub>	La <sub>2</sub> Mo <sub>1.5</sub> W <sub>0.5</sub> O <sub>9</sub>	$\beta$ -phase, La <sub>2</sub> Mo <sub>3</sub> O <sub>12</sub> (traces)	$\beta$ -phase	4.7	1.5	0.3
LMW	La <sub>2</sub> MoWO <sub>9</sub>	$\beta$ -phase La <sub>2</sub> Mo <sub>3</sub> O <sub>12</sub> (traces)	$\beta$ -phase	5.6	1.5	0.32

<sup>a</sup> At room temperature <sup>b</sup> At 630 °C <sup>c</sup> Estimated using Arrhenius equation at 280–450 °C

<sup>d</sup> Determined from VTF equation at 450–700 °C

two elements: the bulk resistance  $R_b$  and the constant phase element ( $CPE$ )<sub>b</sub>; the electrode impedance is observed at high temperatures and comprises only the constant phase element ( $CPE$ )<sub>e</sub>. The total conductivity values were calculated from the  $R_b$  values taking into account geometric parameters of the sample (1):

$$\sigma = \frac{1}{R_b} \left( \frac{t}{S} \right) \quad (1)$$

where  $\sigma$  is the total conductivity (S/cm),  $R_b$  is the bulk resistance,  $t$  is the pellet thickness, and  $S$  is the electrode surface area.

Temperature dependences of the total conductivity for La<sub>2</sub>Mo<sub>2</sub>O<sub>9</sub> and La<sub>2</sub>Mo<sub>1-x</sub>W<sub>x</sub>O<sub>9</sub> samples are shown in Fig. 13. Conductivity of La<sub>2</sub>Mo<sub>2</sub>O<sub>9</sub> shows a sharp increase at around 570 °C due to the structural  $\alpha \rightarrow \beta$  phase transition [1–6], whereas no abrupt conductivity changes are observed for W-doped samples showing stabilization of the cubic phase in agreement with the structural and thermal analysis data. Besides, at temperatures above 400 °C, their conductivity exceeds that of pure La<sub>2</sub>Mo<sub>2</sub>O<sub>9</sub>. In general, the conductivity values of samples obtained in this work ( $4.2\text{--}5.6 \cdot 10^{-3}$  S/cm at 630 °C) are close to those reported earlier in the literature [13–23, 49]. For instance, conductivity of La<sub>2</sub>MoWO<sub>9</sub> ( $5.6 \cdot 10^{-3}$  S/cm at 630 °C) is close to the value of  $\sim 5 \cdot 10^{-3}$  S/cm reported for a similar system by Ge et al. [49].

Usually, two regions of the temperature dependence of conductivity are considered: below and above  $\sim 450$  °C [2, 3]. The conductivity of samples at low temperatures can be satisfactorily fitted by the conventional Arrhenius-type equation (2):

$$\sigma = \frac{A}{T} \exp\left(-\frac{E_a}{kT}\right) \quad (2),$$

where  $A$  and  $E_a$  are the pre-exponential factor and the activation energy, respectively. The activation energy  $E_a$  for W-doped LAMOX is higher as compared with pure La<sub>2</sub>Mo<sub>2</sub>O<sub>9</sub> (Table 1). Its values (1.5 and 1.1 eV, respectively) are close to those obtained in Ref. [16]: 1.4–1.7 eV for La<sub>2</sub>Mo<sub>1-x</sub>W<sub>x</sub>O<sub>9</sub>

and 1.11 and 0.9 eV for  $\alpha$ - and  $\beta$ -La<sub>2</sub>Mo<sub>2</sub>O<sub>9</sub>. The conduction mechanism in the low temperature region is considered as due to the thermally activated oxide ions mobility [2, 3].

At temperatures above 400 °C, a deviation from the linear Arrhenius dependences is observed, presumably caused by the change in the conduction mechanism [13–18]. In this temperature range, the conductivity is satisfactorily described by the empirical Vogel-Tammann-Fulcher (VTF) equation (3) [2, 3, 6, 12]:

$$\sigma = \frac{A}{T} \exp\left(-\frac{E_{\text{VTF}}}{k(T-T_0)}\right) \quad (3),$$

where  $A$ ,  $E_{\text{VTF}}$ , and  $T_0$  are some parameters determined by fitting the experimental data. In such a VTF-type model for LAMOX, the oxide ion migration is assumed to be thermally assisted by the vibration of the cation framework, in which [O1(La)<sub>3</sub>Mo] tetrahedra are able to tilt and rotate with respect to each other, thus opening up a new conduction paths [12, 50]. This leads to a decrease of the activation energy (Table 1) and increase of conductivity due to migration of oxygen from fully occupied O1 sites toward partially occupied O2 and O3 oxygen sites which increase the overall charge carrier concentration.

## Conclusion

La<sub>2</sub>Mo<sub>2-x</sub>W<sub>x</sub>O<sub>9</sub> ( $x = 0.5\text{--}1$ ) samples were synthesized using mechanochemical activation (MA) of starting oxides in a high-power planetary ball mill followed by calcination at 700–900 °C. The study of W-doped LAMOX samples genesis during MA has revealed the formation of mixed lanthanum tungstates-molybdates amorphous precursors. Their calcination at 500° leads to disappearance of amorphous precursors and formation of intermediate La<sub>2</sub>(MoW)<sub>3</sub>O<sub>12</sub> structures. After annealing at 600°, La<sub>2</sub>Mo<sub>2-x</sub>W<sub>x</sub>O<sub>9</sub> appears while a pure cubic phase is formed at 800–900 °C. These results have shown that though the target W-doped molybdates are not formed

directly during mechanical activation, its application facilitates formation of the single phase LAMOX. The cubic  $\beta$ -phase formed from MA products after calcination at 700–950 °C was shown to be stabilized at room temperature.

High-density pellets of WLAMOX ceramics have been obtained already after sintering at 950 °C. W-doped LAMOX possess a higher electrical conductivity as compared with pure  $\text{La}_2\text{Mo}_2\text{O}_9$  at temperatures above 400 °C (i.e.,  $4.7\text{--}5.6 \cdot 10^{-3}$  S/cm at 630 °C).

**Acknowledgments** Support by RSF (Russian Science Foundation) 16-13-00112 Project, Federal Agency of Scientific Organizations (V.45.3.8 Project) and the Russian Ministry of Education and Science is gratefully acknowledged. We are very much thankful to Dr. Kharlamova T. for assistance in samples preparation and Dr. Chesalov Y. for recording IR and Raman spectra.

## References

- Lacorre P, Goutenoire F, Bohnke O, Retoux R, Lalignant Y (2000) Designing fast oxide-ion conductors based on  $\text{La}_2\text{Mo}_2\text{O}_9$ . *Nature* 404:856–858
- Georges S, Goutenoire F, Bohnke O, Steil MC, Skinner SJ, Wiemhufer HD, Lacorre P (2004) The LAMOX family of fast oxide-ion conductors: overview and recent results. *J New Mat Electrochem Systems* 7:51–57
- Malavasi L, Fisher C.A J and Islam MS (2010) Oxide-ion and proton conducting electrolyte materials for clean energy applications: structural and mechanistic features. *Chem Soc Rev* 39: 4370–4387
- Jacquens J, Farrusseng D, Georges S, Viricelle JP, Gaudillere C, Corbel G, Lacorre P (2010) Tests for the use of  $\text{La}_2\text{Mo}_2\text{O}_9$ -based oxides as multipurpose SOFC Core materials. *Fuel Cells* 10:433–439
- Lo JC, Tsai DS, Chen YC, Le MV, Chung WH (2011)  $\text{La}_2\text{Mo}_2\text{O}_9$ -based electrolyte: ion conductivity and anode-supported cell under single chamber conditions. *J Am Ceram Soc* 94:806–811
- Malavasi L, Kim HJ, Billinge SJL, Proffen T, Tealdi C, Flor G (2007) Nature of the monoclinic to cubic phase transition in the fast oxygen ion conductor  $\text{La}_2\text{Mo}_2\text{O}_9$  (LAMOX). *J Am Chem Soc* 129: 6903–6907
- Tealdi C, Chiodelli G, Malavasi L, Flor G (2004) Effect of alkaline-doping on the properties of  $\text{La}_2\text{Mo}_2\text{O}_9$  fast oxygen ion conductor. *J Mater Chem* 14:3553–3557
- Subasri R, Matusch D, Nafe H, Aldinger F (2004) Synthesis and characterization of  $(\text{La}_{1-x}\text{M}_x)_2\text{Mo}_2\text{O}_{9-\delta}$ ;  $\text{M} = \text{Ca}^{2+}$ ,  $\text{Sr}^{2+}$  or  $\text{Ba}^{2+}$ . *J Eur Ceram Soc* 24(1):129–137
- Marrero-Lopez D, Perez-Coll D, Ruiz-Morales J, Canales-Vazquez J, Martin-Sedeno MC, Nunez P (2007) Synthesis and transport properties in  $\text{La}_{2-x}\text{A}_x\text{Mo}_2\text{O}_{9-\delta}$  ( $\text{A} = \text{Ca}^{2+}$ ,  $\text{Sr}^{2+}$ ,  $\text{Ba}^{2+}$ ,  $\text{K}^+$ ) series. *Electrochim Acta* 52:5219–5231
- Georges S, Goutenoire F, Altorfer F, Sheptyakov D, Fauth F, Suard E, Lacorre P (2003) Thermal, structural and transport properties of the fast oxide-ion conductors  $\text{La}_{2-x}\text{R}_x\text{Mo}_2\text{O}_9$  ( $\text{R} = \text{Nd}$ ,  $\text{Gd}$ ,  $\text{Y}$ ). *Solid State Ionics* 161:231–241
- Tsai DS, Hsieh MJ, Tseng JC, Lee HY (2005) Ionic conductivities and phase transitions of lanthanide rare-earth substituted  $\text{La}_2\text{Mo}_2\text{O}_9$ . *J Eur Ceram Soc* 25:481–487
- Corbel G, Suard E, Lacorre P (2011) Structural key of the thermal expansion and the oxide ionic conduction in derivatives of  $\text{La}_2\text{Mo}_2\text{O}_9$ : a temperature-controlled neutron diffraction study of  $\beta\text{-La}_{1.7}\text{Bi}_{0.3}\text{Mo}_2\text{O}_9$ . *Chem Mater* 23:1288–1298
- Corbel G, Lalignant Y, Goutenoire F, Suard E, Lacorre P (2005) Effects of partial substitution of  $\text{Mo}^{6+}$  by  $\text{Cr}^{6+}$  and  $\text{W}^{6+}$  on the crystal structure of the fast oxide-ion conductor structural effects of  $\text{W}^{6+}$ . *Chem Mater* 17:4678–4684
- Jin TY, Madhava Rao MV, Cheng CL, Tsai DS, Hung MH (2007) Structural stability and ion conductivity of the Dy and W substituted  $\text{La}_2\text{Mo}_2\text{O}_9$ . *Solid State Ionics* 178:367–374
- Georges S, Goutenoire F, Lalignant Y, Lacorre P (2003) Reducibility of fast oxide-ion conductors  $\text{La}_{2-x}\text{R}_x\text{Mo}_{2-y}\text{W}_y\text{O}_9$  ( $\text{R} \sim \text{Nd}$ ,  $\text{Gd}$ ). *J Mater Chem* 13:2317–2321
- Georges S, Bohnke O, Goutenoire F, Lalignant Y, Foulletier J, Lacorre P (2006) Effects of tungsten substitution on the transport properties and mechanism of fast oxide-ion conduction in  $\text{La}_2\text{Mo}_2\text{O}_9$ . *Solid State Ionics* 177:1715–1720
- Collado JA, Aranda MAG, Cabeza A, Olivera-Pastor P, Bruque S (2002) Synthesis, structures and thermal expansion of the  $\text{La}_2\text{Mo}_2\text{O}_9$  series. *J Solid State Chem* 167:80–85
- Tealdi C, Chiodelli G, Flor G, Leonardi S (2010) Electrode stability and electrochemical performance of LAMOX electrolytes under fuel cell conditions. *Solid State Ionics* 181:1456–1461
- Chiodelli G, Malavasi L (2013) Electrochemical open circuit voltage (OCV) characterization of SOFC materials. *Ionics* 19:1135–1144
- Marrero-Lopez D, Canales-Vazquez J, Ruiz-Morales J, Irvine J, Nunez P (2005) Electrical conductivity and redox stability of  $\text{La}_2\text{Mo}_2\text{O}_9$  materials. *Electrochim Acta* 50:4385–4395
- Marrero-Lopez D, Canales-Vazquez J, Zhou W, Irvine JTS, Nunez P (2006) Structural studies on  $\text{W}^{6+}$  and  $\text{Nd}^{3+}$  substituted  $\text{La}_2\text{Mo}_2\text{O}_9$  materials. *J Solid State Chem* 179:278–288
- Baque L, Vega-Castillo J, Georges S, Caneiro A, Djurado E (2013) Microstructural and electrical characterizations of tungsten-doped  $\text{La}_2\text{Mo}_2\text{O}_9$  prepared by spray pyrolysis. *Ionics* 19:1761–1774
- Vega-Castillo JE, Ravell UK, Corbel G, Lacorre P, Caneiro A (2014) Thermodynamic stability of  $\text{La}_2\text{Mo}_{2-y}\text{W}_y\text{O}_9$ ,  $\text{La}_2\text{Mo}_{2-y}\text{W}_y\text{O}_{8.96+0.02y}$  and  $\text{La}_7\text{Mo}_{7(2-y)}\text{W}_{7y/2}\text{O}_{30}$  ( $y = 0, 0.5$  and  $1.0$ ). *Dalton Trans* 43:2661–2669
- Haynes WM (ed) (2012-2013) CRC Handbook of Chemistry and Physics. 93rd Edition CRC Press. <https://books.google.ru/books>
- Rojac T, Kosec M (2010) High-energy ball milling. In: Sopickalizer M (ed) Mechanochemical processing of nanopowders, Woodhead Publishing Limited, pp 111–141
- Sepelak V, Duvel A, Wilkening M, Beckerb KD, Heitjans P (2013) Mechanochemical reactions and syntheses of oxide. *Chem Soc Rev* 42:7507–7520
- Zyryanov VV (2008) Mechanochemical synthesis of complex oxides. *Russ Chem Rev* 77:105–135
- Lacorre P, Retoux R (1997) First direct synthesis by high energy ball milling of a new lanthanum molybdate. *J. Solid State Chem* 132:443–446
- Georges S, Goutenoire F, Lacorre P, Steil MC (2005) Sintering and electrical conductivity in fast oxide ion conductors  $\text{La}_{2-x}\text{R}_x\text{Mo}_{2-y}\text{W}_y\text{O}_9$  ( $\text{R}: \text{Nd}, \text{Gd}, \text{Y}$ ). *J Eur Ceram Soc* 25:3619–3627
- Kharlamova T, Pavlova S, Sadykov V, Chaikina M, Kriger T, Lapina O, Khabibulin J, Uvarov N, Frade J, Argiris C (2007) Low-temperature synthesis methods of doped apatite-type lanthanum silicates. *J Chem Eng Jap* 40:1187–1191
- Salavati-Niasari M, Hosseinzadeh G, Davar F (2011) Synthesis of lanthanum hydroxide and lanthanum oxide nanoparticles by sonochemical method. *J Alloys Compd* 509:4098–4103
- Bernal S, Djerdj I, Gamweiner G, Su DS, Niederberger M (2007) Morphology-controlled nonaqueous synthesis of anisotropic lanthanum hydroxide nanoparticles. *J Solid State Chem* 180:2154–2165

33. Le Van T, Che M, Tatibouet JM, Kermarec M (1993) Infrared study of the formation and stability of  $\text{La}_2\text{O}_2\text{CO}_3$  during oxidative coupling of methane on  $\text{La}_2\text{O}_3$ . *J Catal* 142:18–26
34. Adachi G, Imanaka N (1998) The binary rare earth oxides. *Chem Rev* 98:1479–1514
35. Bernal S, Botana FJ, Garcia R, Rodriguez-Izquierdo JM (1987) Behavior of rare earth sesquioxides exposed to atmospheric carbon dioxide and water. *React Solids* 423:23–40
36. Segun L, Figlaz M, Cavagnat R, Lassegues JC (1995) Infrared and Raman spectra of  $\text{MO}_3$  molybdenum trioxides and  $\text{MO}_3 \cdot x\text{H}_2\text{O}$  molybdenum trioxide hydrates. *Spectr Acta A* 51:1323–1344
37. Krishna G, Ravikumar RVSN, Vijaya Kumar T, Ephraim SD, Ranjith B, Pranoy M, Dola S (2016) Investigation and comparison of optical and Raman bands of mechanically synthesised  $\text{MoO}_3$  Nano powders. *Materials Today: Proceedings* 3:4–63
38. Ingham B, Chong SV, Tallon JL (2005) Layered tungsten oxide-based organic-inorganic hybrid materials: an infrared and Raman study. *J Phys Chem B* 109:4936–4940
39. Sungpanich J, Thongtem T, Thongtem S (2012) Large-scale synthesis of  $\text{WO}_3$  nanoplates by a microwave-hydrothermal method. *Ceram Inter* 38:1051–1055
40. Saraiva GD, Luz-Lima C, Freire PTC, Ramiro de Castro AJ, de Sousa PF, Melo EA, Silva JH, Mendes Filho J (2013) Vibrational and structural properties in the dihydrate sodium tungstate and in the dihydrate sodium molybdate crystals. *J Mol Struct* 1033:154–161
41. Mirgorodsky A, Colas M, Smirnov M, Merle-Mejean T, El-Mallawany R, Thomas P (2012) Structural peculiarities and Raman spectra of  $\text{TeO}_2/\text{WO}_3$ -based glasses: a fresh look at the problem. *J Solid State Chem* 190:45–51
42. McEvoy TM, Stevenson KJ (2005) Spatially-resolved imaging of inhomogeneous ion/charge transfer behavior in polymorphous  $\text{MoO}_3$ . I Conductivity and Chemical Mapping using Conductive Probe AFM and Raman Microscopy *Langmuir* 21:3521–3528
43. Diaz-Droguetta DE, El Fara R, Fuenzalida VM, Cabrera AL (2012) In situ-Raman studies on thermally induced structural changes of porous  $\text{MoO}_3$  prepared in vapor phase under He and  $\text{H}_2$ . *Mater Chem Phys* 134:631–638
44. Meng L, Han H, Zhou D, Xia Y, Wang Z, Meng J (2016) Synthesis and luminescence properties of three dimensional architectures of nanostructural  $\text{WO}_3$ . *Optik* 127:3454–3458
45. Pless JD, Kim HS, Smit JP, Wang X, Stair PC, Poeppelmeier KR (2006) Structure of  $\text{Mg}_{2.56}\text{V}_{1.12}\text{W}_{0.88}\text{O}_8$  and vibrational Raman spectra of  $\text{Mg}_{2.5}\text{VWO}_8$  and  $\text{Mg}_{2.5}\text{VMoO}_8$ . *Inorg Chem* 45:514–520
46. Sellemi H, Coste S, Barre M, Retoux R, Ali AB, Lacorre P (2015) Synthesis by the polyol process and ionic conductivity of nanostructured  $\text{La}_2\text{Mo}_2\text{O}_9$  powders. *J All Compd* 653:422–433
47. del Viola C M, Sangra AM, Pedregosa JC (1993) Vibrational spectroscopic characterization of lanthanide molybdates. *J Mat Sci* 28: 6587–6590
48. Hayward SA, Redfern SAT (2004) Thermodynamic nature of and spontaneous strain below the cubic–monoclinic phase transition in  $\text{La}_2\text{Mo}_2\text{O}_9$ . *J Phys Condens Matter* 16:3571–3583
49. Ge L, Guo K, Guo L (2015) Sinterability, reducibility, and electrical conductivity of fast oxide-ion conductors  $\text{La}_{1.8}\text{R}_{0.2}\text{MoWO}_9$  (R = Pr, Nd, Gd and Y). *Ceram Int* 41:10208–10215
50. Lacorre P, Selmi A, Corbel G, Boulard B (2006) On the flexibility of the structural framework of cubic LAMOX compounds in relationship with their anionic conduction properties. *Inorg Chem* 45:627–635